Schweizerischer Erdbebendienst
Service Sismologique Suisse
Servizio Sismico Svizzero
Swiss Seismological Service

ETH *zürich*

SITE CHARACTERIZATION REPORT
SSCN: Schweizerhalle (BL) - Novartis

Clotaire Michel, Paolo Bergamo, Manuel Hobiger, Donat Fäh

Last Modification: 5th October, 2016

Schweizerischer Erdbebendienst (SED)
Service Sismologique Suisse
Servizio Sismico Svizzero
Servizi da Terratrembels Svizzer

ETH Zurich
Sonneggstrasse 5
8092 Zurich
Schweiz
clotaire@sed.ethz.ch

Contents

Summary

The former station SCHC in Schweizerhalle was replaced by the modern free-field SSM-Net station SSCN in the Novartis site in Muttenz. We performed passive and active seismic measurements to characterize this site. The site characterization measurements showed that the fundamental frequency of the structure beneath the station is about 2.6 Hz and is due to the interface between the Opalinus clay soft rock and harder limestone layers at 45 m depth. The alluvial terrace of the Rhine (2 to 8 m depth) and the anthropogenic infill (2 first meters) were clearly characterized as well.

The V_{S30} value there is around 519 m/s and the soil class B.

1 Introduction

In the framework of the second phase of the Swiss Strong Motion Network (SSMNet) renewal project, the existing station SCHC located in the Novartis industrial complex in Muttenz (BL) located in the industrial zone Schweizerhalle, was replaced by a free field station 150 m to the SE (see Fig. 1). It is located in the Rhine valley on an alluvial terrace. The new station SSCN went operational on 21 November 2014. Site characterization was performed using active and passive measurements since the site, relatively stiff and noisy, seemed difficult for passive measurements alone.

Figure 1: Station SSCN (foreground) during the deployment of the geophone line.

2 Geological setting

The site is located in the valley of the Rhine river on an alluvial terrace. According to the geological data of Swisstopo (see Fig. 4), the site SSCN is located in a small graben where Opalinus clay (Aalenian age, middle Jurassic) can be found close to the surface in numerous boreholes of the area, at 8 to 10 m depth. The Opalinus clay is known to be 80 to 100 m thick in Basel (eroded surface here, therefore of lower thickness) and overlays Lower Jurassic limestone (20-40 m thickness) and Triassic age sedimentary rocks. Outside of this small graben structure, the Triassic Trigonodus dolomite is close to the surface, which corresponds to a vertical shift in the order of 200 m. Opalinus clay is known to show a transverse isotropic (TIV) behaviour.

This site is located in the Zone Basel-Ost of the microzonation of Basel.

3 Site characterization using passive measurements

3.1 Measurements and data set

We investigated the local underground structure by passive seismic array measurement which took place on July 5th, 2016. The layout of the seismic array is shown in Fig. 2. The smallest inter-station distance (25 m) is large on purpose, because an underground bunker is present below the field and therefore does not allow to investigate the small wavelengths. The active measurement was designed to complement this expected lack of information at high frequencies.

The parameters of the array are given in Table 1. For these measurements 12 Nanometrics Centaur dataloggers named NR42 to NR49 and NR52 to NR55 and 16 Lennartz 3C 5 s seismometers were available. Each datalogger can record on 2 ports A (channels EH1, EH2, EH3 for Z, N, E directions) and B (channels EH4, EH5, EH6 for Z, N, E directions). Time synchronization is ensured by GPS. The sensors were placed on a metal tripod and positioned, when possible, in a 20 cm deep hole for better coupling with the ground.

The sensor coordinates were measured using a differential GPS device (Leica Viva GS10), including only a rover station and using the Real Time Kinematic technique provided by Swisstopo. It allows an absolute positioning with an accuracy better than 4 cm on the Swissgrid. Two points (SCN201 and SCN304) located close to buildings could be measured with an accuracy of only 10 cm.

Table 1: Seismic array measurement in Schweizerhalle.

Array name	Number of sensors	Minimum interstation distance [m]	Aperture [m]	Recording time [min]
SCN	16	25	240	236

The largest time windows were extracted, for which all the sensors of the array were correctly placed and the GPS synchronization was ensured. The time frame when active measurements were performed was excluded. Recordings during the active measurement may also be extracted from the data. Large peaks due to anthropogenic disturbances are noticed at many frequencies, as everywhere in the Basel area, especially a 1.13 Hz peak already noticed in many measurements. The overall quality of the recordings is very good considering they have been performed in an industrial site. The only exception is point SCN301, located along the main road, where the noise on Z and E components is elevated probably due to tilt of the sensor when cars and trucks are passing. Points SCN000 and possibly SCN102 are located on top of the underground bunker but its effect is not clearly visible on the spectra.

Orientations of the sensors was checked by maximizing the correlation with the central station at low frequencies (Poggi et al., 2012b). The error were generally lower than 5° except for points SCN304 and SCN305 where is was about 20°.

Figure 2: Layout of the array measurements at site SSCN.

3.2 Measurement results

3.2.1 H/V curves

The H/V curves all show a similar shape. The effect of the underground bunker on the H/V ratios is clear above 8 Hz (filtering) for SCN000. They show a fundamental peak around 2.6 Hz that can be compared to other measurements performed in the surroundings and present in the SED database (Fig. 4). They highlight the fact that the area of the measurement, in between two faults, has a relatively homogeneous behaviour, while outside of this small graben structure (covered by the alluvial terrace), the fundamental frequency is higher. Quaternary sediments (alluvial terrace), less than 10 m thick in this area, are not correlated with this fundamental peak. It corresponds therefore to a layer within Jurassic and Triassic layers.
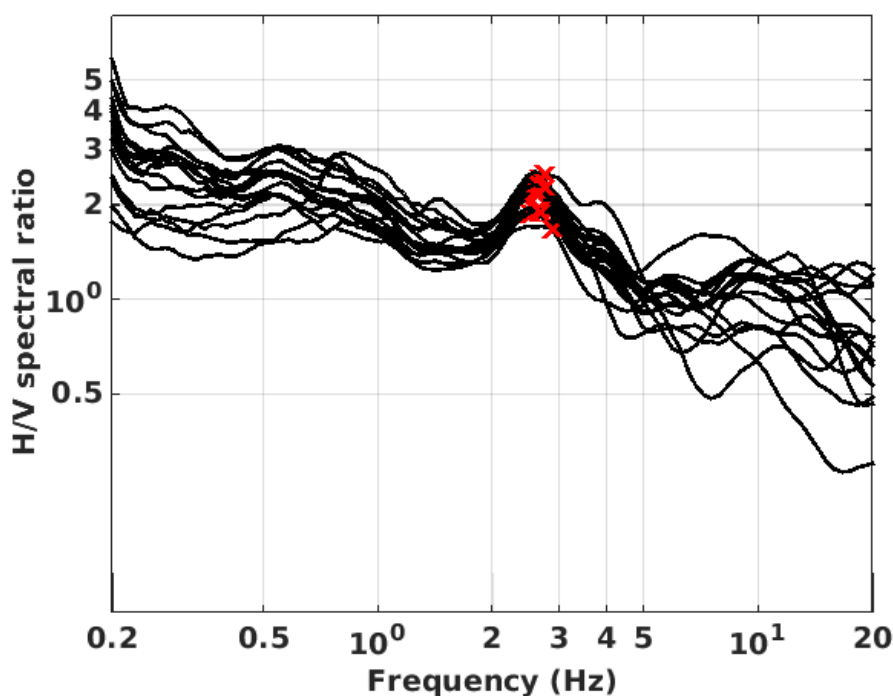

Figure 3: Comparison of H/V spectral ratios (time-frequency analysis code V. Poggi) between the different points of the array.

Moreover, all the methods to compute H/V ratios are compared at point SCN104, close to SSCN in Fig. 5, in which the classical methods were divided by $\sqrt{2}$ to correct from the Love wave contribution (Fäh et al., 2001). The classical and TFA methods match above the fundamental peak. The 3C FK analysis (Capon method) matches in terms of shape but shows much lower amplitude. It hardly has resolution down to the peak. The sign of the ellipticity shows that the polarization of Rayleigh waves is retrograde above 4 Hz. It is however not clear if the singularity found at 4 Hz is real. The comparison with the other curves does not show a clear match.

In addition, the temporary station XSCH2 installed during 1 week in the basement of the building in the north of the SSCN station was reprocessed using the H/V method (Fig. 6). It nicely show the 2.5 Hz peak but in addition a small peak at 0.54 Hz that could
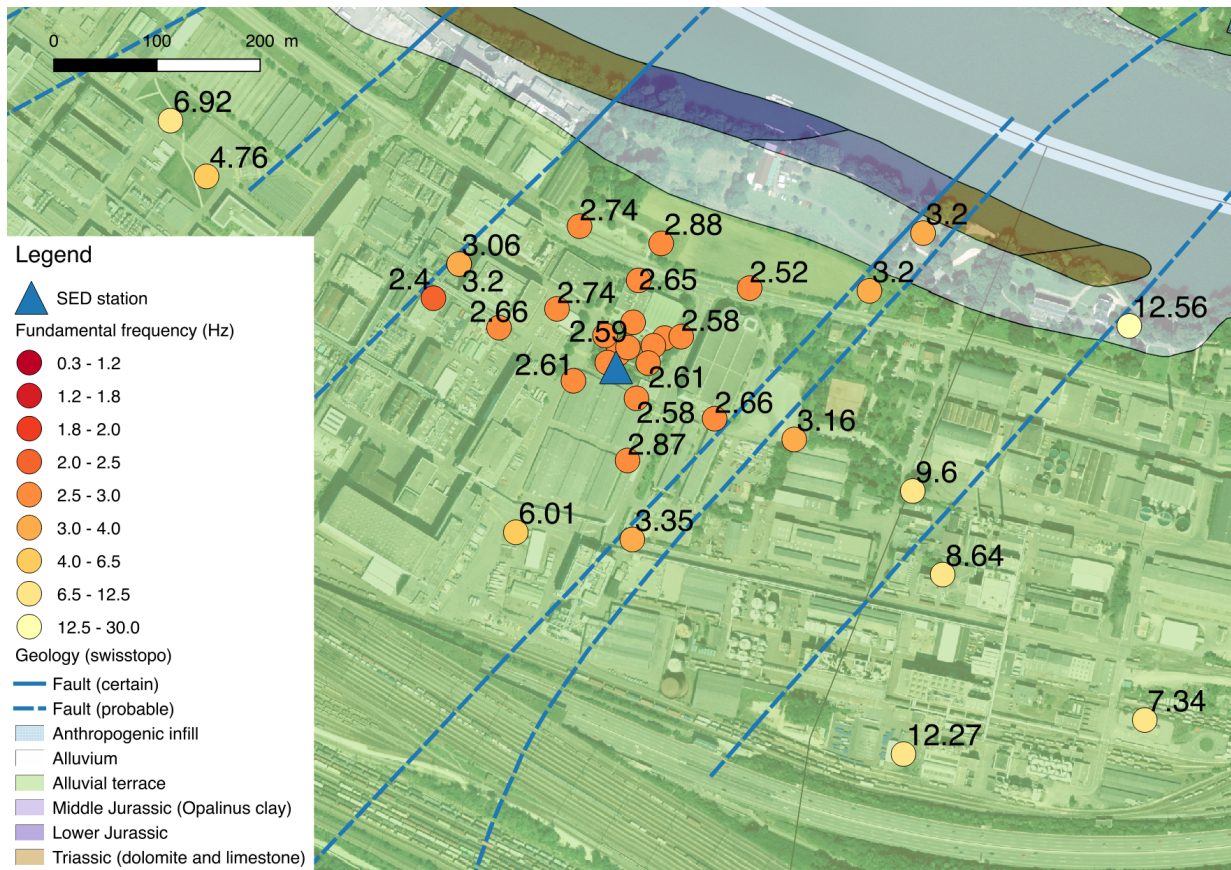
Figure 4: Maps of the fundamental peaks in the H/V ratios from this measurement and SED database superimposed on the simplified geological map of the area.

show the presence of deeper resonance in the rock layers. This peak is also seen on the array data (Fig. 5).

The fundamental peak at the SSCN station is therefore at 2.6 Hz, with a peak amplitude around 2.5.
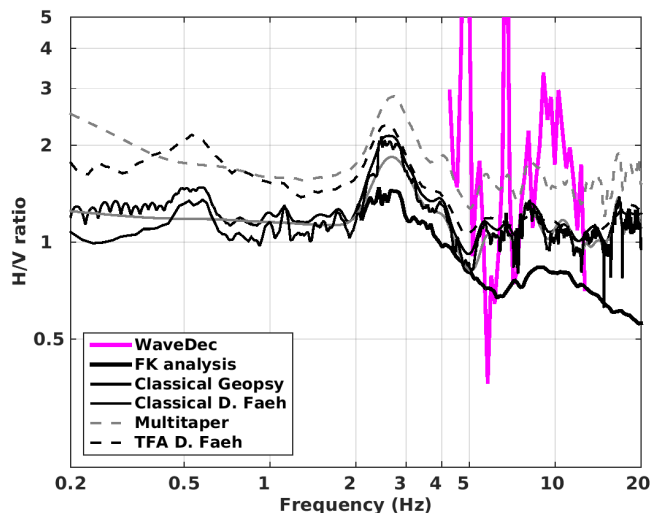

Figure 5: H/V spectral ratios for point SCN104 using the different codes. Classical methods were divided by $\sqrt{2}$.
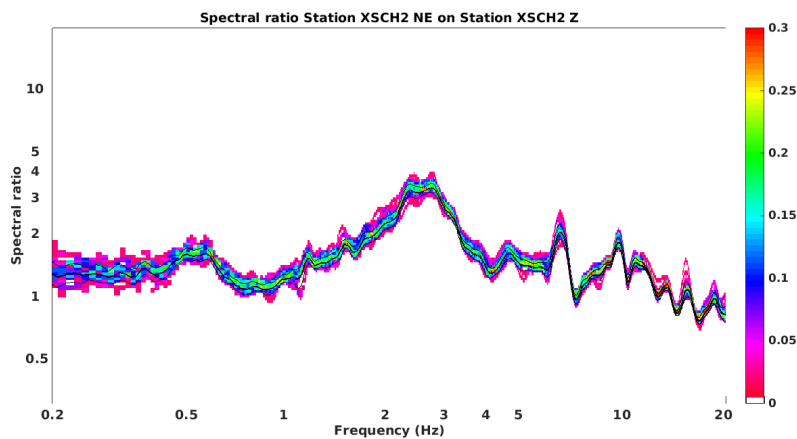

Figure 6: H/V spectral ratio of the temporary station XSCH2 installed in the basement of the building located N of SSCN during one week. The color scale refers to the probabiliy of occurence over time.

3.2.2 Polarization analysis

Polarization analysis on the array data was performed to check for 2D resonance using the method of Burjánek et al. (2010). All points (Fig. 7) show a flatter motion at 2.6 Hz as also retrieved with the H/V ratios with a slight but consistent polarization in the direction of the faults in Fig. 4. We can assume that there is no strong 2D behaviour of the small graben structure at this site, but a 2D resonance cannot be completely excluded.
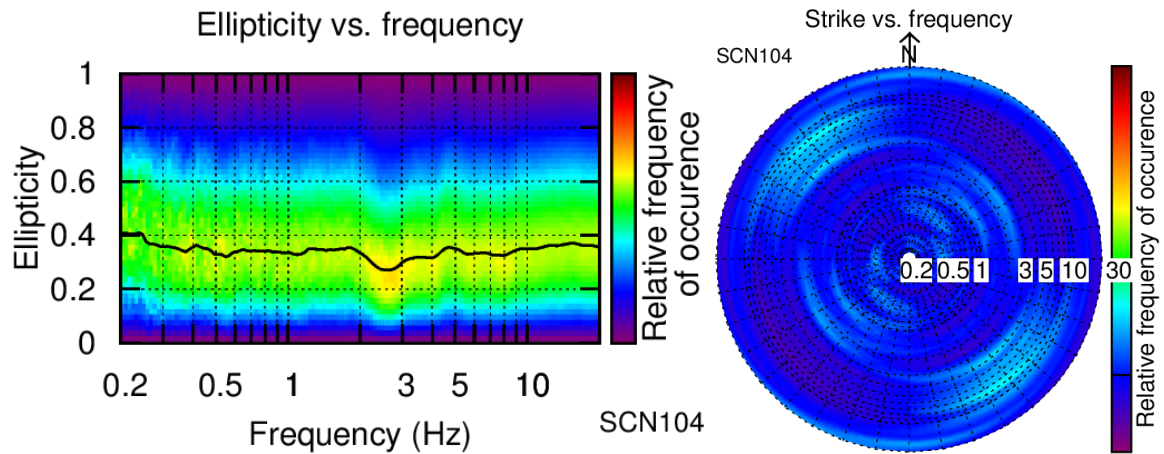

Figure 7: Polarization analysis at point SCN104. Left: Ellipticity (a trough in the ellipticity corresponds to polarized motion). Right: Strike of the polarization.

3.3 3-component high-resolution FK

The results of the 3-component high-resolution FK analysis (Poggi and Fäh, 2010) are shown in Fig. 8. The fundamental modes of Rayleigh and Love waves are clearly determined from this analysis between 3.2 and 17 Hz. From the radial component, the fundamental mode is unclear, but what can be interpreted as the second higher modes can be distinguished.

The ellipticity curve determined with the 3-component HRFK analysis is comparable to the H/V analysis, but with lower amplitudes (Fig. 5).
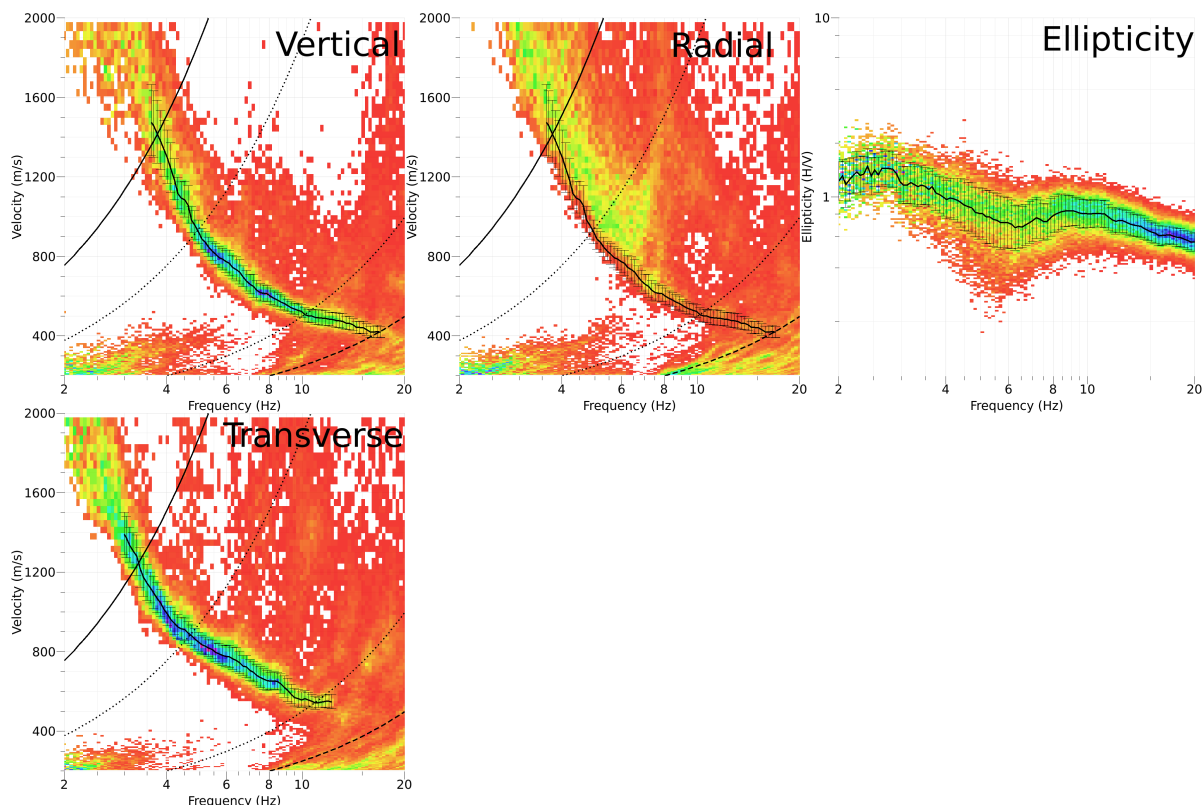

Figure 8: Dispersion curves obtained from the 3C HRFK analyses. The picked curves correspond to the final interpretation (see following sections).

3.4 Wavedec

WaveDec (Maranò et al., 2012) has also been used to process the array data. This technique estimates the properties of multiple waves simultaneously with a maximum likelihood approach in the time domain. It was applied assuming the presence of 3 waves.

The fundamental Love and Rayleigh waves dispersion curves could be picked (Fig. 9) and are compared to the other analyses in section 5. The ellipticity of Rayleigh waves (Fig. 10) is relatively unclear but it seems that the sense of rotation changes at about 4 Hz (trough). The comparison with other proxys for the ellipticity curve (Fig. 5) is however not convincing.
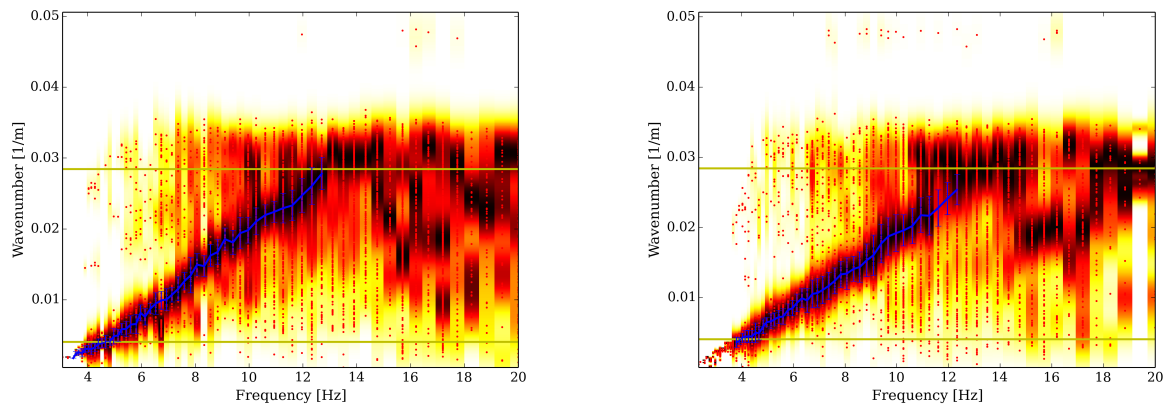
Figure 9: Rayleigh and Love wave dispersion curves obtained with the WaveDec technique (Maranò et al., 2012). The yellow lines indicate the theoretical array resolution limits.
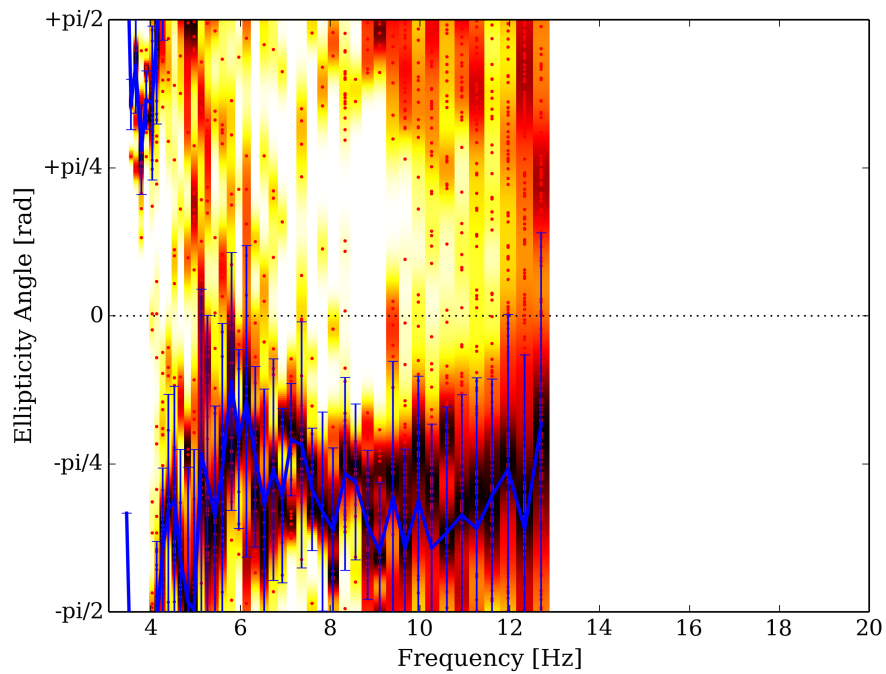

Figure 10: Rayleigh ellipticity curve obtained with the WaveDec technique (Maranò et al., 2012).

4 Site characterization using active measurements

As the the targeted station (SSCN) is located within an operating chemical plant, an active seismic survey, besides passive seismic measurements, was carried out. The purpose was providing seismic characterization of the shallow subsurface in close proximity to the station within a depth range (0-10 m depth) that is poorly investigated by, or out of reach of, noise recording techniques. Thanks to the use of controlled sources in proximity to the recording array, active measurements would ensure signal coverage within a frequency band (approx. 15 - 100 Hz) that was expected to be consistently affected by undesired noise sources related to plant activities. For the sake of a comprehensive subsurface seismic characterization, both multichannel analysis of surface waves (MASW; Park et al., 1999) and P-wave refraction (Redpath, 1973) surveys were conducted.

4.1 Equipment

We used two sets of eight three-component geophones (4.5 Hz corner frequency). Each geophone set was connected to a Geode datalogger; the two Geodes were coupled for time synchronization. The seismic source was 5 kg sledgehammer hitting a metal plate. Along the handle of the hammer, a trigger sensor was firmly fastened (and then connected to the Geodes) to ensure a convenient start of the acquisition window.

4.2 Geometry of the acquisition array

Due to logistical restrictions, the subsurface beneath the spacious lawn area in Fig. 11 being occupied by a one-storey underground structure (bunker), the acquisition spread was deployed on a relatively limited strip of soil close to the SSCN station (Fig. 11). The 16 geophones (see previous section) were arranged in a linear array, spaced by 1 m intervals. Receivers were firmly coupled to the ground thanks to metal spikes attached to the base of the geophones. Shot points were placed in line with the receivers spread: i) externally to the geophones array, at both ends, for MASW acquisitions (2 m offset between source and the closest receiver); ii) along the geophone array (at both extremities and at an intermediate location) for P-wave refraction acquisition (Fig. 11).
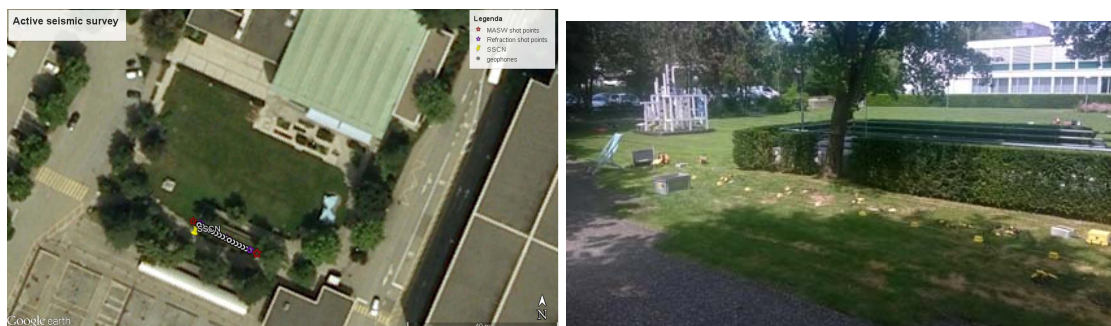

Figure 11: map representing the location of the active seismic array and of the station SSCN and picture of the deployment of the seismic array.

4.3 Acquisition

For both MASW and P-wave refraction acquisitions, seismic data were acquired using a sampling interval of $62.5\,\mu s$. The window length was $0.5\,s$ (corresponding to 8000 samples) and a pre-trigger delay of -0.01 s was employed. At each source point, 10 hammer blows were successively shot; at each shot, the recordings from all geophones were saved in a separate .sg2 file. In Fig. 12, the seismic traces acquired having placed the source at a MASW (a) and at a refraction (b) shot point are displayed. Despite the high level of noise caused by the activities of the chemical plant, data quality appears to be relatively good, the useful seismic events (surface waves and P-wave first break arrivals) being clearly recognizable in the seismic sections. In Fig. 12, in the leftmost panel, the surface wave train (labelled SW) and P-wave first break arrivals (labelled P) are highlighted.

4.4 Processing

4.4.1 Pre-processing

Seismic traces generated by different shots, the seismic source being positioned at the same location, were summed - or stacked - in time domain. The scope of this operation is enhancing the coherent seismic events generated by the controlled seismic source (sledgehammer blow), and at the same time minimizing the incoherent noise anyhow present in the recordings (Foti et al., 2014). "Stacked" seismic sections, with greater signal-to-noise ratio, were hence obtained (Fig. 13). To preserve the effectiveness of the stacking operation, the vertical component of the seismic traces at shorter offset were cross-correlated to ensure an adequate synchronization among the seismograms to be later superimposed (Fig. 14). The small shifts that are evident in Fig. 14a can be ascribed to a non-ideal behavior of the trigger device.

4.4.2 P-wave refraction processing

P-wave first break arrival times were manually picked on the stacked seismograms representing the vertical component of soil surface vibration. As anticipated in section 4.2, three recording configurations were considered for P-wave refraction, the seismic source being positioned at both ends of the geophone array and at an intermediate location. Fig. 15 represents the seismic sections on which the picking operation was carried out, as well as the picked travel time curves, or hodocrones.
As shown in Fig. 15, the hodocrones appear to be approximately symmetrical, i.e. the P-wave travel time depends only on the source-to-receiver offset distance and not on the position of the shot point. This suggests a 1D geometry (no lateral variations) for the shallow subsurface below the active seismic array.

4.4.3 MASW processing

Vertical and longitudinal component seismograms from MASW acquisitions, considering both single shot and stacked seismic sections, were processed by means of a 2D f-k (frequency-wavenumber) transform (Socco and Strobbia, 2004), so to obtain a conversion of the recorded sets of traces from time - offset to frequency - wavenumber domain. The energy maxima in the retrieved f-k panels correspond to the propagation of Rayleigh
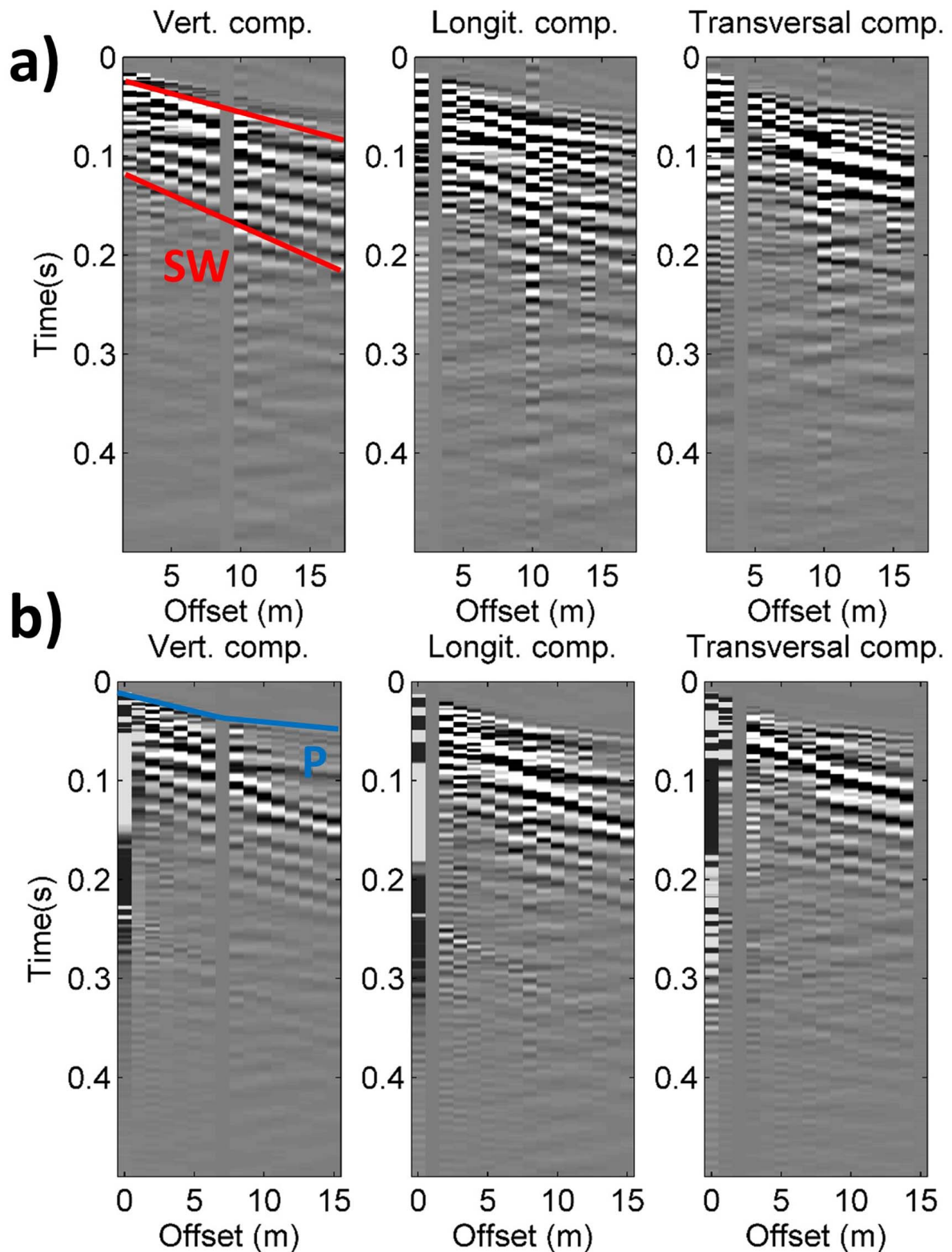
Figure 12: a) seismic traces (vertical, longitudinal and transversal component) recorded by the geophones spread having placed the seismic source in the MASW shot point north-west of the array (Fig. 11). In the leftmost panel, the surface wave train is highlighted. b) seismic traces (vertical, longitudinal and transversal component) recorded by the geophones spread having placed the seismic source in the refraction shot point at the north-west end of the array line (Fig. 11). In the leftmost panel, the P-wave first break arrivals are highlighted.
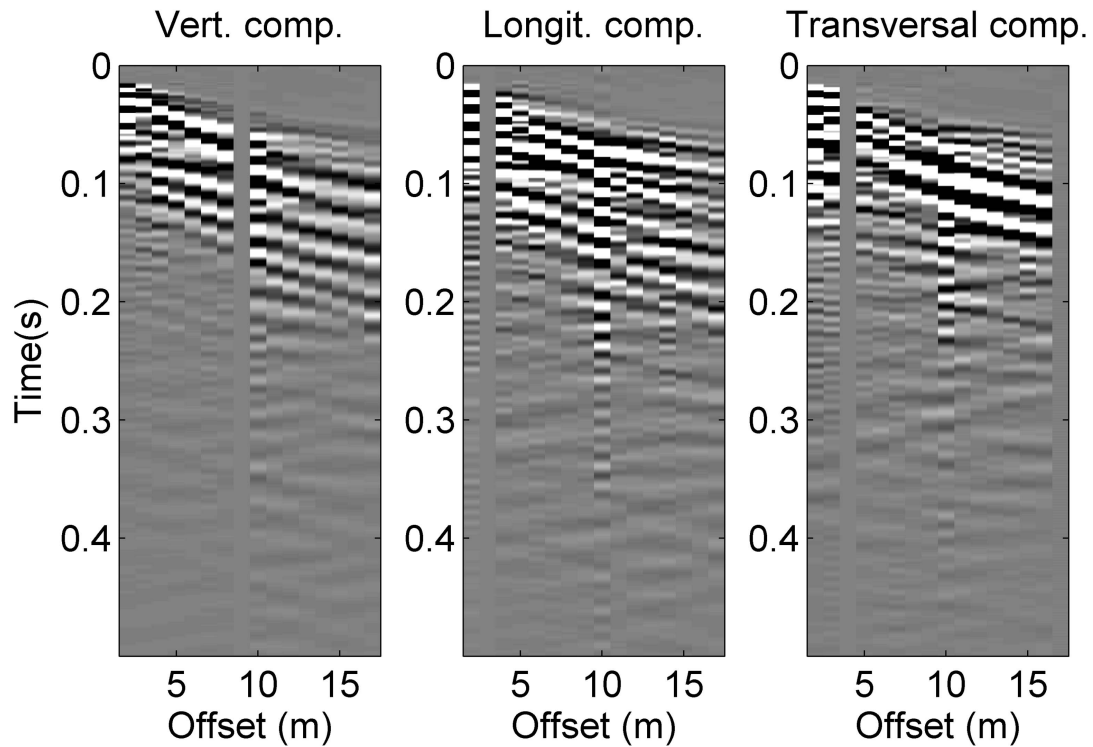
16

Figure 13: stacked seismic sections (vertical, longitudinal and transversal component) obtained by summing the 10 different seismograms recorded after positioning the source at the MASW shot point north-west of the geophones array (same of Fig. 12a; compare Fig. 13 with Fig. 12a).
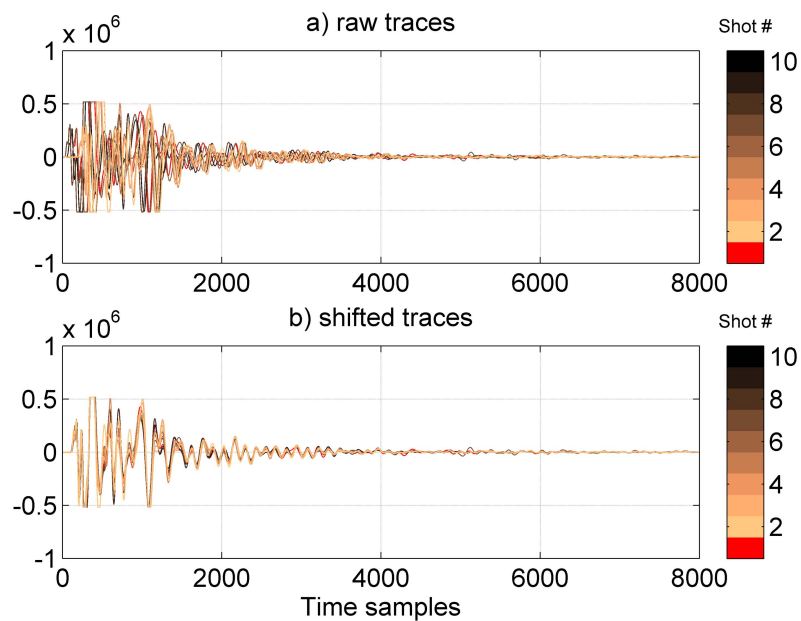

Figure 14: Retrieving the optimal synchronization among seismic traces before stacking. a) raw seismic traces (vertical component) recorded at offset = 2 m at the 10 different shots carried out by positioning the source at the MASW shot point north-west of the array; b) synchronized traces after the shifts for an optimal synchronization were retrieved via cross-correlation.
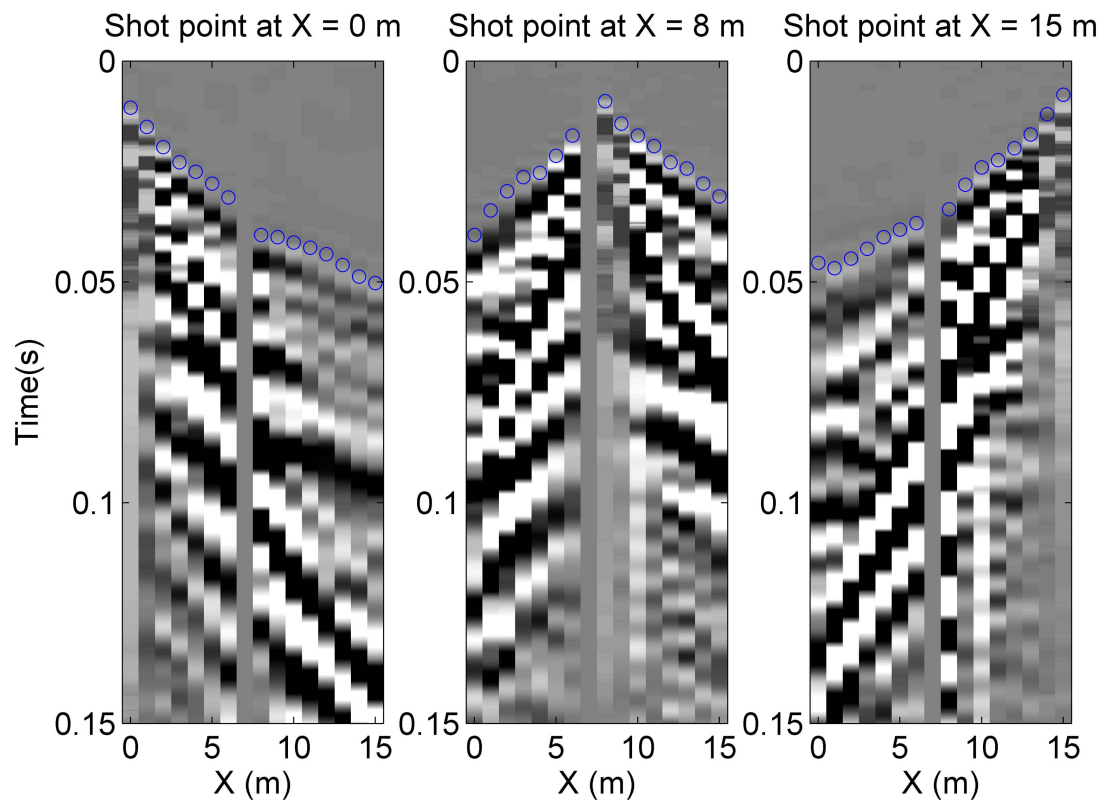
Figure 15: Picking of P-wave first break arrival times (blue dots) on vertical component seismograms obtained after the stacking of raw traces. The X coordinate reference system is longitudinal to the receiver spread and progresses from north-west (first geophone, X = 0) to south-east (16th geophone, X =15 m).

waves and they depict the Rayleigh waves dispersive behavior (Socco and Strobbia, 2004; Foti et al., 2014). The maxima in the f-k panels from stacked seismic sections were picked by manually defining regions of interest in the f-k domain and then automatically identifying the peaks, frequency by frequency, within the selected areas Fig. 16. The defined regions of interest were also automatically applied to the f-k spectra from single shot seismograms. Hence for each shooting configuration and for each considered component (vertical or longitudinal) we obtained:

i) a set of f-k maxima, retrieved from the stacked seismic section, that define the corresponding dispersion curve (circles in Fig. 17a);

ii) ten sets of f-k maxima , each of them derived from a single shot seismogram, that define the experimental uncertainty for the dispersion curve introduced in i (dots in Fig. 17a).

This processing procedure follows the scheme described by Socco et al. (2009); Boiero and Socco (2010). As shown in Fig. 16 and Fig. 17, the obtained dispersion curves are multimodal, i.e. they comprise other modes of propagation of Rayleigh waves besides the fundamental. The fundamental mode extends with few interruptions in the frequency band 15 - 100 Hz, gently increasing the phase velocity from 160 to 400 m/s as the frequency decreases. Other dispersion curve branches, attributed to higher modes, are present within 30-120 Hz (with phase velocities as high as 800 m/s), although they do not span the whole frequency interval. The maximum observable wavelength is 30 m, coinciding with the upper array resolution limit (set to twice the array length, Socco and Strobbia, 2004).

The dispersion curves from the four considered datasets (vertical and longitudinal components of the two off-end shootings) show good reciprocal consistency, aligning along coherent modal branches. This similarity, particularly among curves from opposite shooting configurations, confirms the hypothesis, inferred from the observation of P-wave travel times (section 4.4.2), of a substantially 1D geometry for the subsurface beneath the active seismic array.

The agreement among the four dispersion curves from stacked seismic sections (circles in Fig. 17a), allows combining them, via averaging, into a single dispersion curve, representative of Rayleigh wave propagation in the subsoil below the active seismic array (Fig. 17b). As earlier anticipated, the phase velocity data from single shot dispersion curves (dots in Fig. 17a) were exploited to define the experimental uncertainties (error bars in Fig. 17b, computed as the standard deviation of the relevant population of phase velocity data). As expected, the width of the uncertainty intervals increases as frequency decreases (from an average of 3.5% at 100 Hz to 13% below 20 Hz), but it generally reaches limited values (70% of uncertainties lie below 5% of the corresponding velocity value).

The attribution of the dispersion curve branches above the fundamental mode to the first and second higher modes (Fig. 17b) was based on a preliminary inversion (not included in this report) of active dispersion data performed with the Monte Carlo multimodal algorithm proposed by Maraschini and Foti (2010). This algorithm does not require a priori mode numbering and allows identifying the most reliable data point attribution.
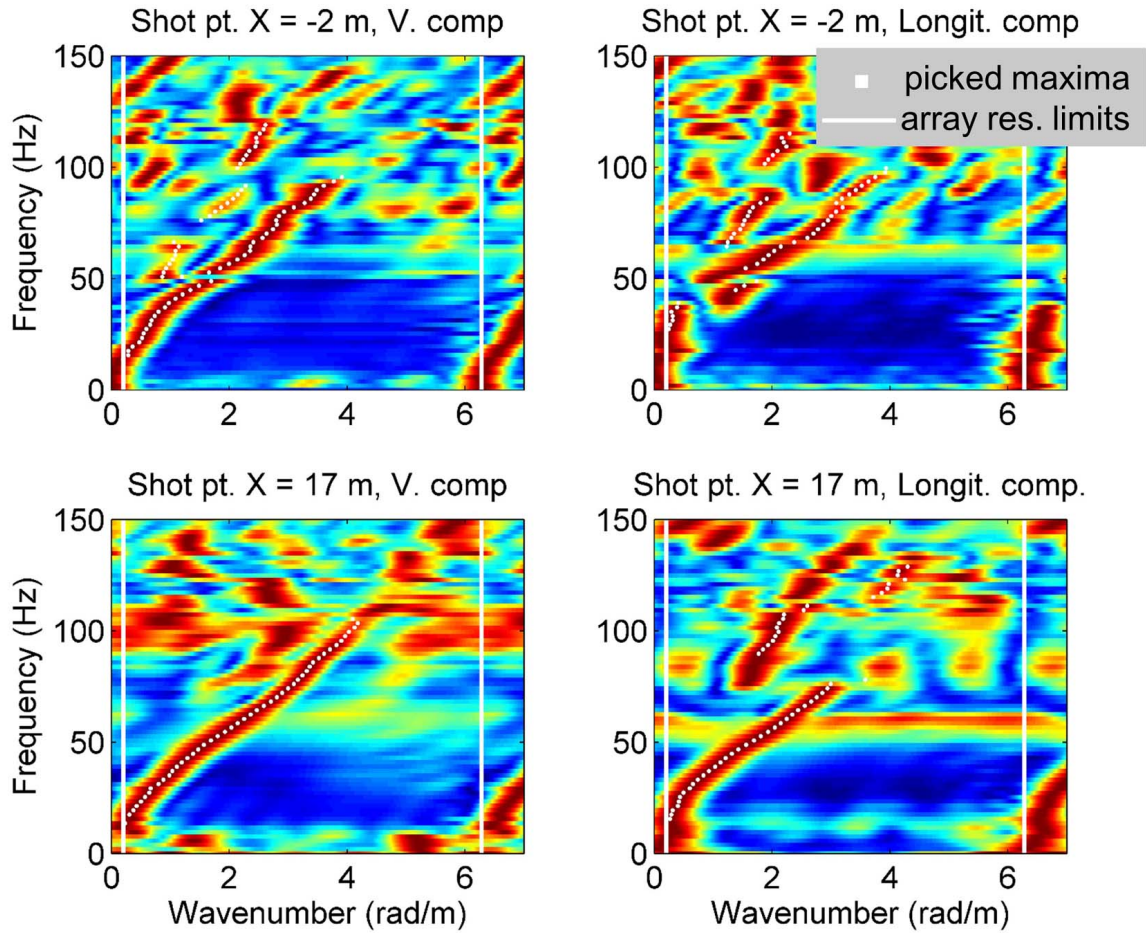
Figure 16: normalized f-k spectra obtained from vertical and longitudinal components of stacked seismic sections of MASW recording configurations. Top panels: f-k spectra relevant to the shot point north west of the array (source at X = -2 m). Bottom panels: f-k spectra relevant to the the shot point south east of the array (source at X = 17 m).
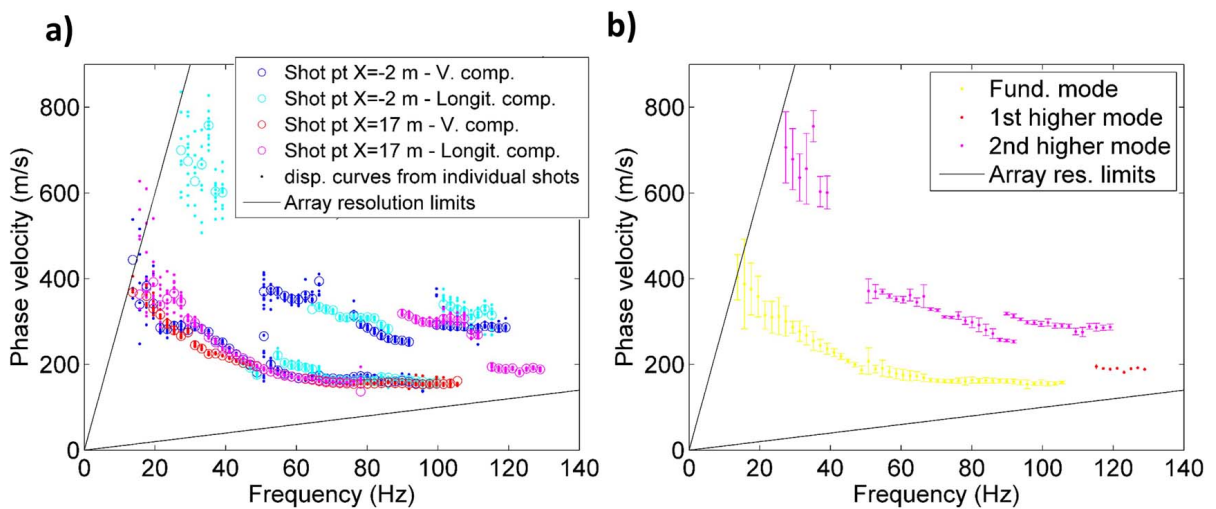

Figure 17: obtained dispersion curves. a) dispersion curves derived from stacked seismic sections (circles) and single shot seismograms (dots); b) average dispersion curve with uncertainties.

4.5 P-wave refraction interpretation

P-wave refraction data (section 4.4.2) were interpreted with the method of intercept time analysis (Reynolds, 2011). Following the hypothesis of a 1D geometry for the shallow subsurface (sections 4.4.2 and 4.4.3), the hodocrones obtained from refraction processing were collapsed in a single travel-time curve in time-offset domain (black circles in Fig. 18a). Examining Fig. 18, the travel time curve appears to be divided into two portions: one extending at offsets $< 9\,m$, with steeper slope, and interpreted as the segment of direct arrivals; the second part of the hodocrone, at offsets $> 9\,m$, has a gentler slope and it gathers the refracted arrival times. Applying the intercept time equations, the obtained VP profile is hence a simple two layer model, with a surficial layer having VP = 306 m/s and thickness = 2.15 m, resting on a halfspace with VP = 550 m/s (Fig. 18c). Unfortunately, the limited length of the receiver spread and the relatively high P-wave velocities of the subsurface do not allow larger investigation depths. The velocity change at 2.15 m depth can be realistically interpreted as the interface between the surficial fill material surrounding the underground built structure mentioned in section 4.2 and the deeper natural soil. We underline that this feature is presumably local, proper of the subsurface illuminated by active surveys, and it is not representative of the whole area investigated by combined passive and active measurements. Hence also the configuration of the dispersion curve points with related wavelengths (particularly $\lambda < 2.15\,m$; fundamental mode $> 75\,Hz$, higher modes $> 110\,Hz$) is likely to be considered a local characteristic as well.
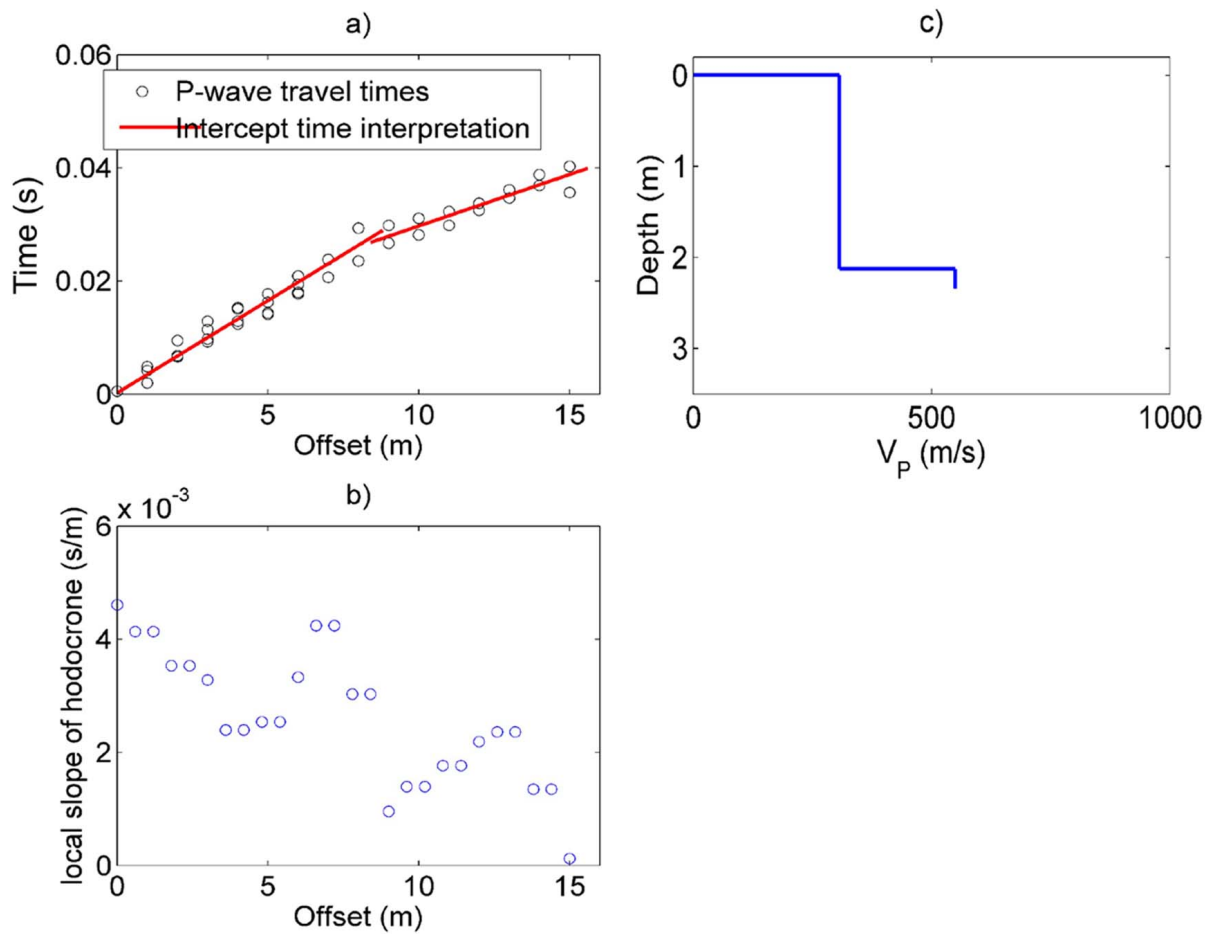
Figure 18: P-wave travel time interpretation. a) travel time data points and linear fitting of the two hodocrone segments. b) local slope of the travel time curve, evaluated with a moving window. c) obtained P-wave velocity model.

5 Interpretation of the surface wave data and inversion

Fig. 19 gives an overview of the dispersion curves determined from the active and passive datasets. The curves are retrieved between 3.2 and more than 100 Hz with velocities ranging from about 1300 m/s at 4 Hz down to 150 m/s at 100 Hz for the fundamental Rayleigh mode.
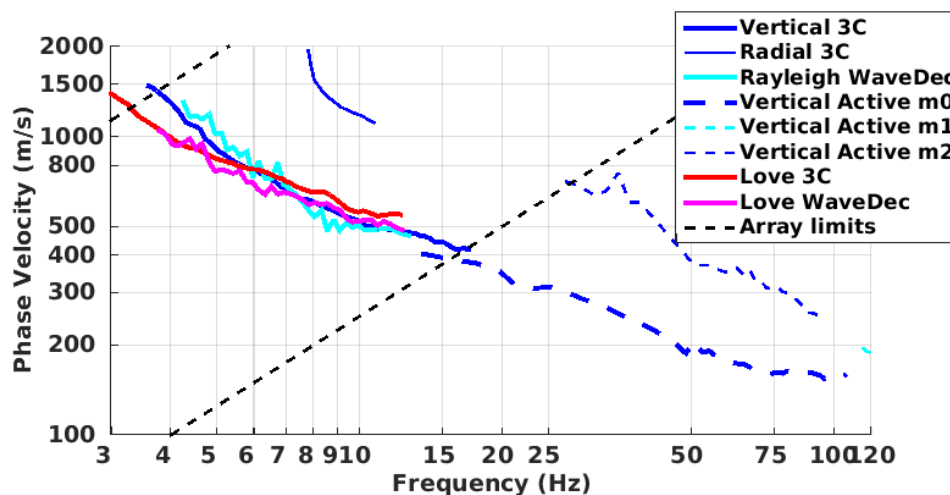

Figure 19: Picked dispersion curves from passive and active measurements.

The inversion of the surface waves properties into 1D velocity profiles was performed using the Improved Neighborhood Algorithm (NA) (Wathelet, 2008) implemented in the Dinver software.

5.1 Misfit function

For the inversion, the Rayleigh fundamental and second higher modes dispersion curves from the passive and active measurements, the Love fundamental dispersion curve from the passive measurement, a part of the ellipticity curve at point SCN104 (TFA Poggi) and the fundamental frequency at 2.6 Hz were used as simultaneous targets without standard deviation. The ellipticity information was given low weight (0.1) compared to the dispersion curves.
All curves were resampled using 100 points between 1 and 100 Hz in log scale.

5.2 Parametrization of the model space

The velocity was assumed to increase with depth. A posteriori, we showed that no velocity inversion is needed to explain the observed data. The Poisson ratio was inverted in each layer in the range 0.2-0.4, up to 0.47 between 3 and 10 m, within the groundwater table. The density was assumed to be 1800 kg/m^3 in the 2 first meters, 2000 kg/m^3 below and 2500 kg/m^3 in the rock. Inversions with free layer depths as well as fixed layer depths were performed. 5 layers are necessary to explain the dispersion curves, especially a velocity increase between 100 and 200 m. 5 independent runs of 5 different parametrization schemes (4 and 5 layers over a half space and 12 and two times 13 layers with fixed depth) were performed.

23

5.3 Results

Examples of retrieved ground profiles for these two strategies are presented in Fig. 20. When comparing to the target curves (Fig. 21), dispersion curves are generally well reproduced. Ellipticity is not matching well with the H/V curve that is only a proxy for Rayleigh wave ellipticity, but the overall shape is consistent. For further elaborations, the best models of these 25 runs were selected (see section 6.1). In their surficial portion, the selected Vp profiles match the model from P-wave refraction (section 4.5, Fig. 22).
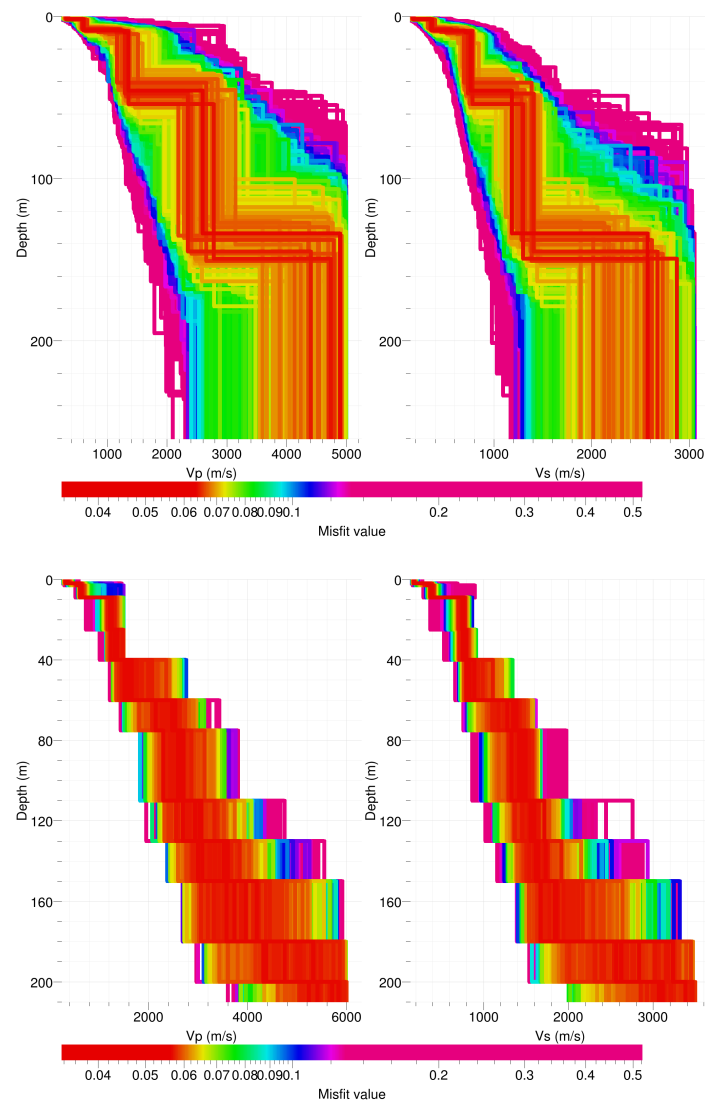

Figure 20: Inverted ground profiles at SSCN in terms of V_p and V_s; top: free layer depth strategy; bottom: fixed layer depth strategy.
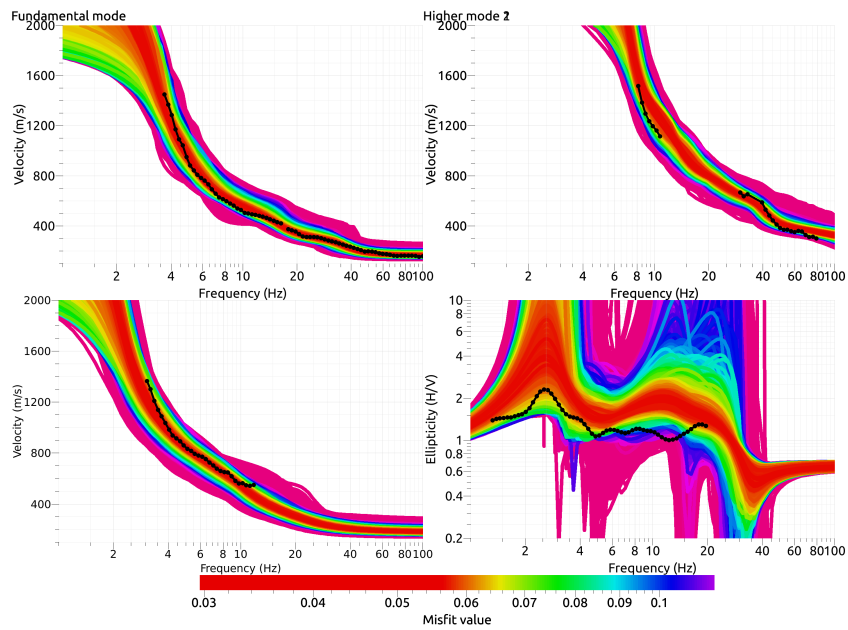
Figure 21: Comparison between inverted models and measured Rayleigh (top row;fundamental mode: left, second higher mode: right) and Love (bottom row left) modes and corresponding ellipticity (bottom row, right) at SSCN site.
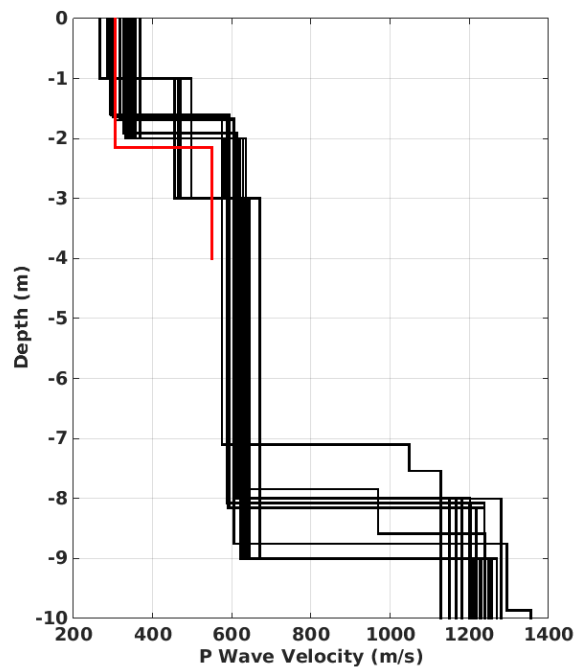

Figure 22: P-wave velocity profiles of the 25 selected models (black) compared to the refraction results (red) over the 10 first meters.

6 Interpretation of the velocity profiles

6.1 Velocity profiles

The first two meters of the profile shows low velocities (about 170 m/s). Below, the velocity is around 370 m/s until 8 m depth. This layer corresponds to the alluvial terrace of the Rhine (Quaternary) and its thickness matches the expectations. It is surprisingly not visible on the H/V ratios (expected at 12 Hz). The following layer has a velocity of 725 m/s and is probably the Opalinus clay of Jurassic age, until about 45 m depth. At this depth, a more compact rock at 1500 m/s is found. This contrast corresponds to the fundamental peak on the H/V curve at about 2.6 Hz. This rock is most probably dolomite and limestone from Jurassic and Triassic age. At 150 m depth, the velocity starts to increase significantly. It should be noticed that Permian rocks are expected in this range of depth, before reaching the basement, most probably a couple of hundreds of meters below (Michel et al., 2016).
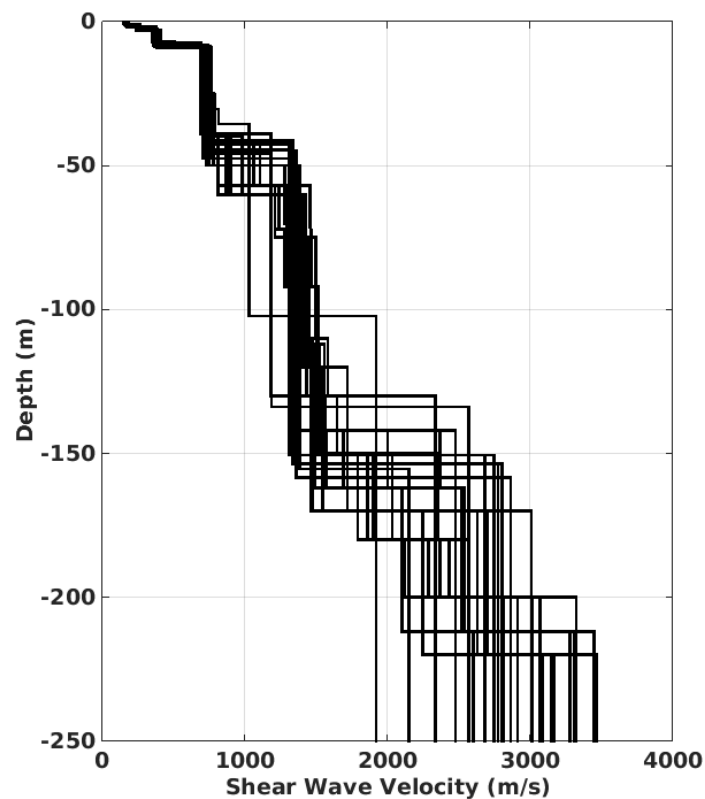

Figure 23: Shear-wave velocity profiles of the 25 selected models.

The distribution of the travel time average velocities at different depths was computed from the selected models. $V_{s,30}$ is found to be 519 m/s, which corresponds to class B in the Eurocode 8 (CEN, 2004) and the SIA261 (SIA, 2014).

6.2 Quarter-wavelength representation

The quarter-wavelength velocity approach (Joyner et al., 1981) provides, for a given frequency, the average velocity at a depth corresponding to 1/4 of the wavelength of interest. It is useful to identify the frequency limits of the experimental data (minimum frequency in dispersion curves at 3 Hz and in the ellipticity at 2.6 Hz here). The results using this proxy show that the dispersion curves constrain the profiles down to 55 m and the ellipticity down to 64 m (Fig. 24). Moreover, the quarter wavelength impedance-contrast introduced by Poggi et al. (2012a) is also displayed in the figure. It corresponds to the ratio between two quarter-wavelength average velocities, respectively from the top and the bottom part of the velocity profile, at a given frequency (Poggi et al., 2012a). It shows a trough (inverse shows a peak) at the resonance frequency.
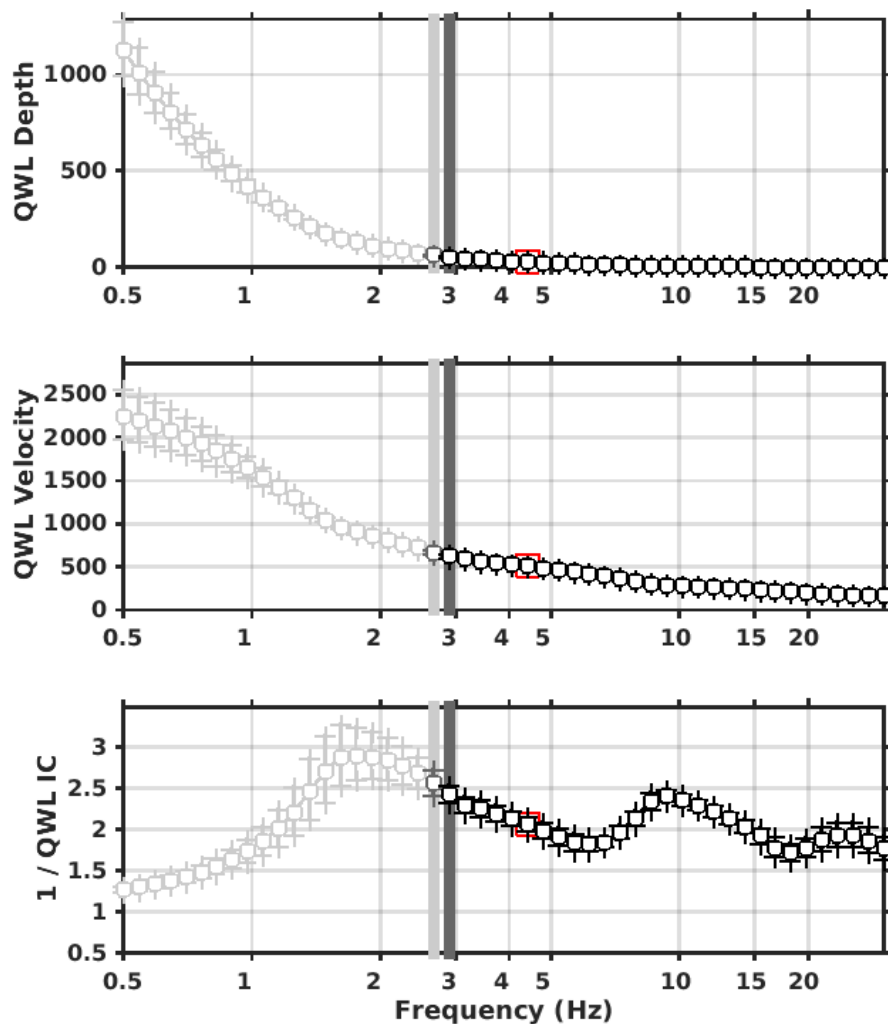

Figure 24: Quarter wavelength representation of the velocity profile for the selected velocity profiles (top: depth, center: velocity, bottom: inverse of the impedance contrast). The black curves are constrained by the dispersion curves, the light grey curves are not constrained by the data. The red square corresponds to V_{S30}.

6.3 SH transfer function

The theoretical SH-wave transfer function for vertical propagation (Roesset, 1970) is computed from the selected profiles. It is corrected with respect to the Swiss Reference Rock model (Poggi et al., 2011) following Edwards et al. (2013). It is compared to the amplification function obtained by empirical spectral modelling (ESM) (Edwards et al., 2013; Michel et al., 2014, 2016). Although the empirical amplification for station SSCN is only based on few events so far, theoretical SH transfer function of the retrieved profiles matches well this observed amplification function (Fig. 25).
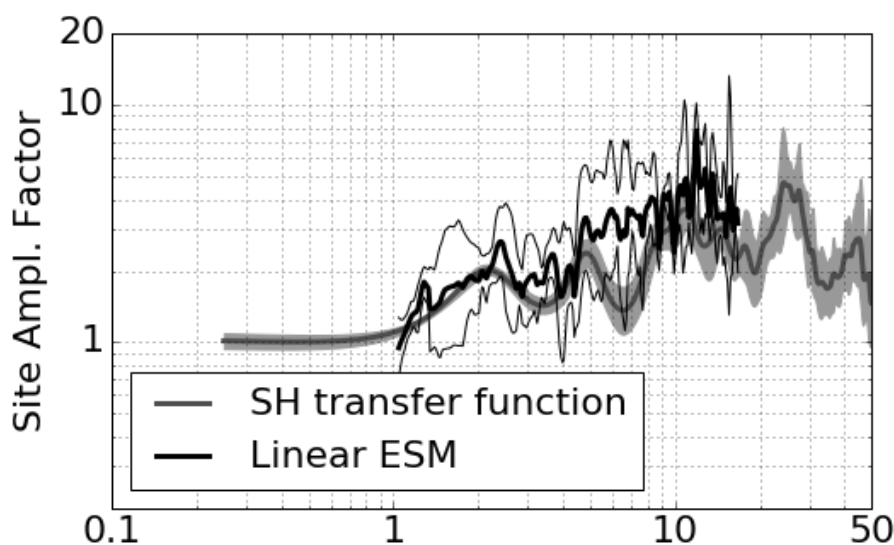

Figure 25: Comparison between the modeled SH transfer function for the selected velocity profiles and the empirical amplification (ESM) measured at station SSCN (with standard deviation).

7   Conclusions

The active and passive measurements presented in this study were successful in deriving a velocity model for the site Schweizerhalle Novartis (SSCN station). The first two meters of the profile show velocities of about 170 m/s. Below, the alluvial terrace of the Rhine is present until 8 m depth and shows a velocity of 370 m/s. The following layer has a velocity of 725 m/s and is probably the Opalinus clay of Jurassic age, until about 45 m depth. At this depth, a more compact rock at 1500 m/s is found. This contrast corresponds to the fundamental peak on the H/V curve at about 2.6 Hz. The interpretation of the following rock layers in terms of geology was not possible. The station is located in a small graben of Opalinus clay that can be clearly identified with the H/V measurements.

$V_{s,30}$ is 519 m/s, which would correspond to ground type B in the Eurocode 8 (CEN, 2004) and SIA261 (SIA, 2014). The theoretical 1D SH transfer function computed from the inverted profiles matches the observed amplification at the station under earthquake.

Acknowledgements

References

Boiero, D. and Socco, L. V. (2010). Retrieving lateral variations from surface wave dispersion curves. *Geophysical Prospecting*, 58(6):977–996.

Burjánek, J., Gassner-Stamm, G., Poggi, V., Moore, J. R., and Fäh, D. (2010). Ambient vibration analysis of an unstable mountain slope. *Geophysical Journal International*, 180(2):820–828.

CEN (2004). *Eurocode 8: Design of structures for earthquake resistance - Part 1: General rules, seismic actions and rules for buildings*. European Committee for Standardization, en 1998-1: edition.

Edwards, B., Michel, C., Poggi, V., and Fäh, D. (2013). Determination of Site Amplification from Regional Seismicity : Application to the Swiss National Seismic Networks. *Seismological Research Letters*, 84(4).

Fäh, D., Kind, F., and Giardini, D. (2001). A theoretical investigation of average H/V ratios. *Geophysical Journal International*, 145(2):535–549.

Foti, S., Lai, C. G., Rix, G. J., and Strobbia, C. (2014). *Surface Wave Methods for Near-Surface Site Characterization*. CRC Press, Taylor & Francis Group LLC.

Joyner, W. B., Warrick, R. E., and Fumal, T. E. (1981). The effect of Quaternary alluvium on strong ground motion in the Coyote Lake, California, earthquake of 1979. *Bulletin of the Seismological Society of America*, 71(4):1333–1349.

Maranò, S., Reller, C., Loeliger, H. A., and Fäh, D. (2012). Seismic waves estimation and wavefield decomposition: Application to ambient vibrations. *Geophysical Journal International*, 191(1):175–188.

Maraschini, M. and Foti, S. (2010). A Monte Carlo multimodal inversion of surface waves. *Geophysical Journal International*, 182(3):1557–1566.

Michel, C., Edwards, B., Poggi, V., Burjánek, J., Roten, D., Cauzzi, C., and Fäh, D. (2014). Assessment of Site Effects in Alpine Regions through Systematic Site Characterization of Seismic Stations. *Bulletin of the Seismological Society of America*, 104(6):2809–2826.

Michel, C., Fäh, D., Edwards, B., and Cauzzi, C. (2016). Site amplification at the city scale in Basel (Switzerland) from geophysical site characterization and spectral modelling of recorded earthquakes. *Physics and Chemistry of the Earth, Parts A/B/C*.

Park, C. B., Miller, R. D., and Xia, J. (1999). Multichannel analysis of surface waves. *Geophysics*, 64(3):800–808.

Poggi, V., Edwards, B., and Fäh, D. (2011). Derivation of a Reference Shear-Wave Velocity Model from Empirical Site Amplification. *Bulletin of the Seismological Society of America*, 101(1):258–274.

Poggi, V., Edwards, B., and Fäh, D. (2012a). Characterizing the Vertical-to-Horizontal Ratio of Ground Motion at Soft-Sediment Sites. *Bulletin of the Seismological Society of America*, 102(6):2741–2756.

Poggi, V. and Fäh, D. (2010). Estimating Rayleigh wave particle motion from three-component array analysis of ambient vibrations. *Geophysical Journal International*, 180(1):251–267.

Poggi, V., Fäh, D., Burjánek, J., and Giardini, D. (2012b). The use of Rayleigh-wave ellipticity for site-specific hazard assessment and microzonation: application to the city of Lucerne, Switzerland. *Geophysical Journal International*, 188(3):1154–1172.

Redpath, B. B. (1973). Seismic refraction exploration for engineering site investigations. Technical report, Explosive Excavation Research Laboratory, Livermore, California.

Reynolds, J. M. (2011). *An Introduction to Applied and Environmental Geophysics*. John Wiley & Sons, Ltd.

Roesset, J. (1970). Fundamentals of soil amplification. In Hansen, R. J., editor, *Seismic Design for Nuclear Power Plants*, pages 183–244. M.I.T. Press, Cambridge, Mass.

SIA (2014). *SIA 261 Einwirkungen auf Tragwerke*. Société suisse des ingénieurs et des architectes, Zurich, Switzerland.

Socco, L. and Strobbia, C. (2004). Surface-wave method for near-surface characterization: a tutorial. *Near Surface Geophysics*, 2(22):165–185.

Socco, L. V., Boiero, D., Foti, S., and Wisén, R. (2009). Laterally constrained inversion of ground roll from seismic reflection records. *Geophysics*, 74(6):G35–G45.

Wathelet, M. (2008). An improved neighborhood algorithm: Parameter conditions and dynamic scaling. *Geophysical Research Letters*, 35(9):1–5.